Fractal Analysis of the ERCAOS Dataset

Michael D. Abercrombie[1], **V. S. Rao Gudimetla**[2], **Daniel R. Abercrombie**[1], **and Roman Tillman**[3]
[1]*The Boeing Company,* [2]*Air Force Research Laboratory,*
[3]*United States Space Force*

ABSTRACT

Current Directed Energy Directorate programs using active imaging, including that of space-based objects, and long-range laser communications are currently limited by the degree to which the physics of the atmosphere is understood. Improving the models used to describe strong atmospheric turbulence offers a means to advance these critical capabilities and to develop a deeper understanding of the physical processes driving these fluctuations.

To characterize atmospheric turbulence near the Air Force Research Laboratory's (AFRL) Maui Space Surveillance Complex, located at 10,023 feet above sea level on Haleakalā, over 400 GB of optical wavefront data collected during the Extended Range Comprehensive Atmospheric Optical Sensor (ERCAOS) campaign in April 2019 has been investigated for fractal properties. This analysis was performed using the well-known box counting algorithm and was run on Hokule'a, the Maui High Performance Computing Center's (MHPCC) IBM POWER8 system. Additional rescaled range analysis and multifractal detrended fluctuation analysis (MF-DFA) has been performed on this data to further understand the variability of turbulence over time. This work supports previous findings that atmospheric turbulence is multifractal in nature.

1. INTRODUCTION

Atmospheric turbulence has been found to exhibit fractal properties, specifically multifractal properties, with a scale-dependent structure that can be characterized using standard fractal analysis techniques [1, 2, 3]. These techniques includes methods of measuring the fractal dimension and other quantities that aim to identify and describe fractal structure, characterizing the complexity and scaling properties of various physical systems.

It is suspected that optical wavefront measurements offer a means to observe and characterize the turbulence through which the optical source is being viewed. This paper describes efforts to determine the fractal dimension and time-series variability of wavefront intensity data collected during the ERCAOS campaign.

2. DATASET

The Extended-Range Comprehensive Atmospheric Optics Sensing (ERCAOS) dataset is the result of a campaign conducted during April 2019 as part of a collaboration between researchers from the University of Dayton and AMOS personnel. A polychromatic beacon (PCB) transmitter projecting at wavelengths of $\lambda = 532$ nm, $\lambda = 1064$ nm, and $\lambda = 1550$ nm was stationed at the NOAA Mauna Loa Observatory on Hawaii Island's Mauna Loa volcano at an elevation of 3397 meters above sea level. Multiple 30.5 cm-diameter Meade telescopes located at the Maui Space Surveillance Complex on the summit of Haleakala were used as receivers, employing various sensors for data collection. These telescopes were stationed at an elevation of 3058 meters, with a total beam propagation path of 149.2 km from the source.

Wavefront measurements were stored in HDF5 files as $N_f \times 244 \times 240$ arrays where each of the N_f frames were collected at a constant frame rate for a total duration of 30 seconds. Data was collected by a pupil-plane photo array and a focal-plane photo-array with a 4×4 lenslet array in the optical path. For this analysis only data collected in pupil plane mode was considered. This includes $\lambda = 532$ nm wavelength data collected at 211 frames per second collected using a Mission-Oriented Reconfigurable Speckle-Average Phase Retrieval (MORSAPR) wavefront sensor and $\lambda = 1064$ nm wavelength data collected at 59 frames per second using a Multi-Aperture Phase Reconstruction (MAPR) wavefront sensor[4, 5].

Approved for public release; distribution is unlimited. Public Affairs release approval #AFRL-2023-4326.

3. METHODS

Multiple methods have been applied to search for, and characterize, the fractal properties of atmospheric turbulence imprinted on a traversing optical wavefront. First, wavefront intensity was investigated via the box counting approach to quantify fractal scaling by measuring the two-dimensional fractal dimension D_2 of each collection [6]. Secondly, rescaled range analysis was performed to study temporal variability. This was then extended following the generalized multifractal detrended fluctuation analysis (MF-DFA) algorithm described by Kantelhardt et al. to search for multifractal properties in the wavefront data [7].

3.1 Measuring Fractal Dimension

To measure the fractal dimension of ERCAOS wavefront intensity data via the box counting algorithm, the first step was to assign iso-scalar surfaces to the data. For each frame of each collection iso-scalar surfaces were identified as regions with pixels above a threshold value T determined by the factor a relative to the maximum value in the input image frame I by

$$T = \max(I)/a. \tag{1}$$

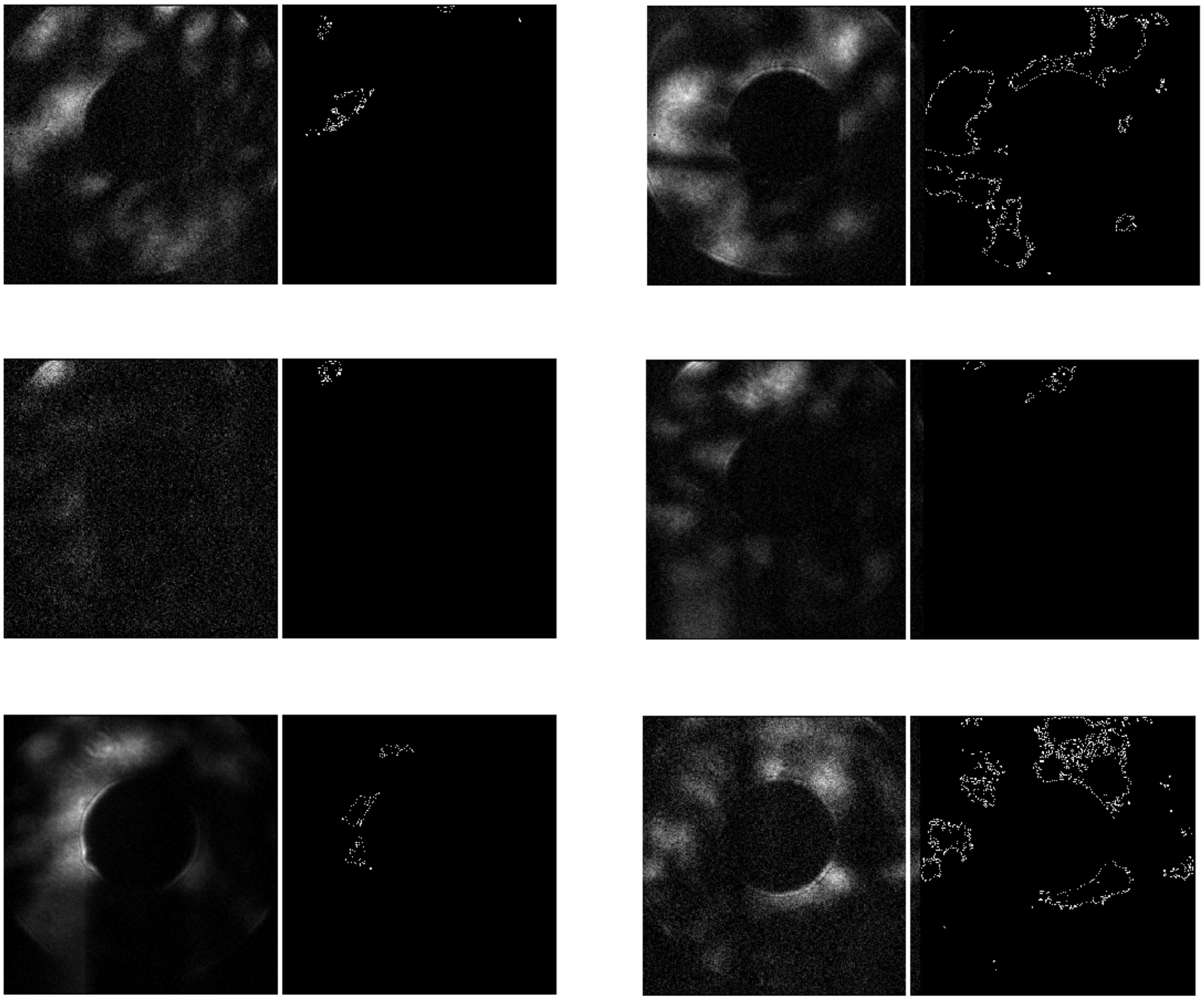

Fig. 1: Six example frames from the ERCAOS dataset showing wavefront intensity collected in the pupil plane configuration and the corresponding iso-scalar surface boundaries (to the right of each wavefront image).

The classical box-counting algorithm was applied to determine the fraction of boxes containing part of the surface contours as a function of box size. Box sizes of 2, 4, 8, 16, 32, and 64 were used for threshold factors of 2.0 and 4.0 and the results were written to an SQLite database with each entry containing a file id designator, the threshold factor a, the box size s, the frame number, and the box count fraction.

The fractal dimension D_d provides a measure of the geometric complexity for a physical system, such as atmospheric turbulence [1]. For a 2-dimensional system, such as single frame optical wavefront images,

$$D_2 \equiv -\frac{d \log N_2(\lambda)}{d \log \lambda} \tag{2}$$

where $N_2(\lambda)$ is the number of boxes containing contour boundaries and λ is the length scale (or box size) being considered.

An example of a $\log\lambda$ vs $\log N_2(\lambda)$ plot for a single file is shown in Figure 2 for both threshold values used. Here fractal dimensions D_2 of 0.452 and 0.493 are displayed as lines of best fit for iso-scalar threshold factors of 2.0 and 4.0, respectively. Measured fractal dimensions for ERCAOS data from the 3rd, 5th, and 9th of April 2019 are provided in Figures 3-5, separated by day, iso-scalar surface threshold parameters, and sensor used for data collection. Each data point represents the measurement made from one HDF5 file (see Figure 2). Only data collected in the pupil plane configuration were considered for the fractal dimension analysis.

Inspection of these fractal dimension measurements shows a dependence on iso-scalar surface threshold for data collected using the MORSAPR sensor that is far less pronounced for data collected with the MAPR sensor. For the April 5th and April 9th, fractal dimension D_2 measured with a threshold factor of $a = 4.0$ was, on average, 0.490 ± 0.217 and 0.451 ± 0.202 larger, respectively, than D_2 measured when the threshold factor was taken as $a = 2.0$ for MORSAPR data collections. For the same dates, fractal dimension was 0.020 ± 0.036 and 0.090 ± 0.027 larger when $a = 4.0$ for data collected using the MAPR sensor. The difference ΔD_2 for each collection on these dates is shown in Figure 6. It is unclear if this difference is wavelength dependent, or if it can be explained by some other phenomena.

3.2 Rescaled Range Analysis

Next, rescaled range analysis was performed on the ERCAOS dataset to characterize the apparent variability of the wavefront intensity over the time-span of data collections. This variability is quantified by the Hurst exponent, which describes the increase in the rescaled range as the time series increases. To make this measurement for a

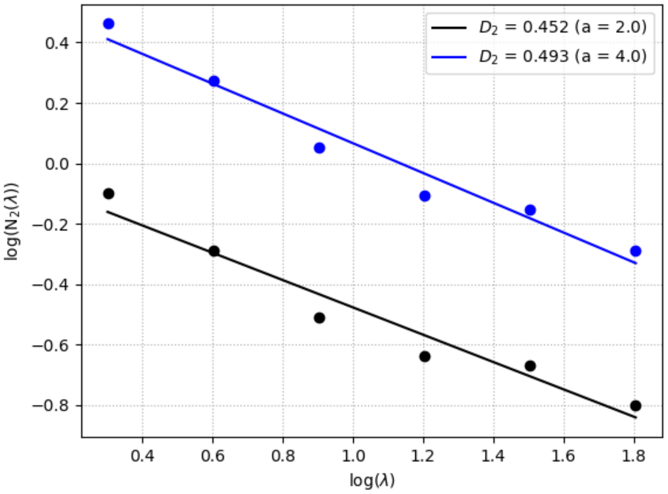

Fig. 2: Log-log plot of the boundary coverage as a function of box size. Data points and linear least-squares fits are shown for threshold factors of $a = 2.0$ (in black) and $a = 4.0$ (in blue).

Approved for public release; distribution is unlimited. Public Affairs release approval #AFRL-2023-4326.

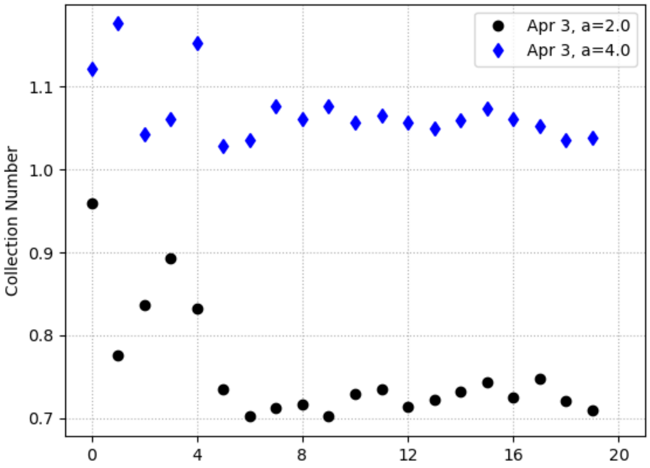

Fig. 3: Fractal dimension over subsequent collections made on 3 April 2019 for threshold factors $a = 2.0$ and 4.0. There is an average fractal dimension difference of 0.312 ± 0.061 depending on the threshold chosen.

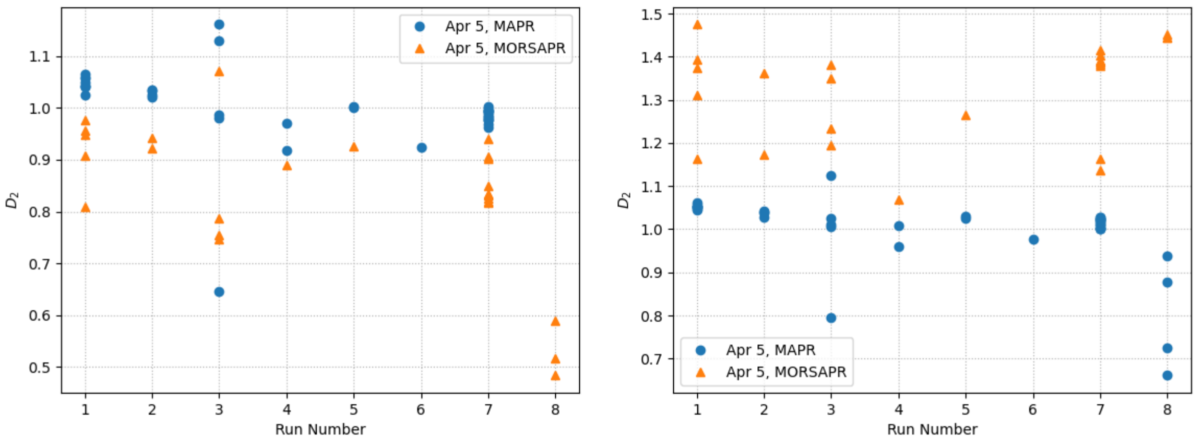

Fig. 4: Fractal dimension over subsequent collections made on 5 April 2019 for threshold factors $a = 2.0$ (left) and 4.0 (right).

one-dimensional time series, the cumulative deviate series z_i is determined from a sequence of partial summations

$$z_i = \sum_{k=1}^{i} (y_k - \bar{y}_s)^2 \tag{3}$$

where $\bar{y}_s$ is the sub-sample mean of the series of y_k values. The range series R_t is determined by

$$R_t = \max\{z_i\} - \min\{z_i\} \tag{4}$$

and the rescaled range is then

$$(R/S)_s = R_s/\sigma_s \tag{5}$$

where sample standard deviation σ_s is given by

$$\sigma_s = \left[\frac{1}{M}\sum_{k=1}^{M} (y_k - \bar{y}_s)^2\right]^{1/2}. \tag{6}$$

Approved for public release; distribution is unlimited. Public Affairs release approval #AFRL-2023-4326.

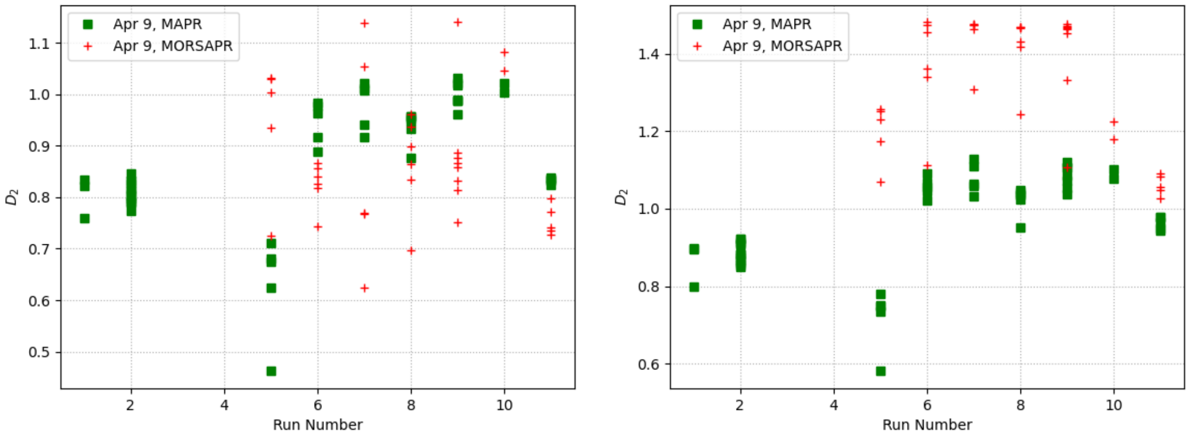

Fig. 5: Fractal dimension over subsequent collections made on 9 April 2019 for threshold factors $a = 2.0$ (left) and 4.0 (right).

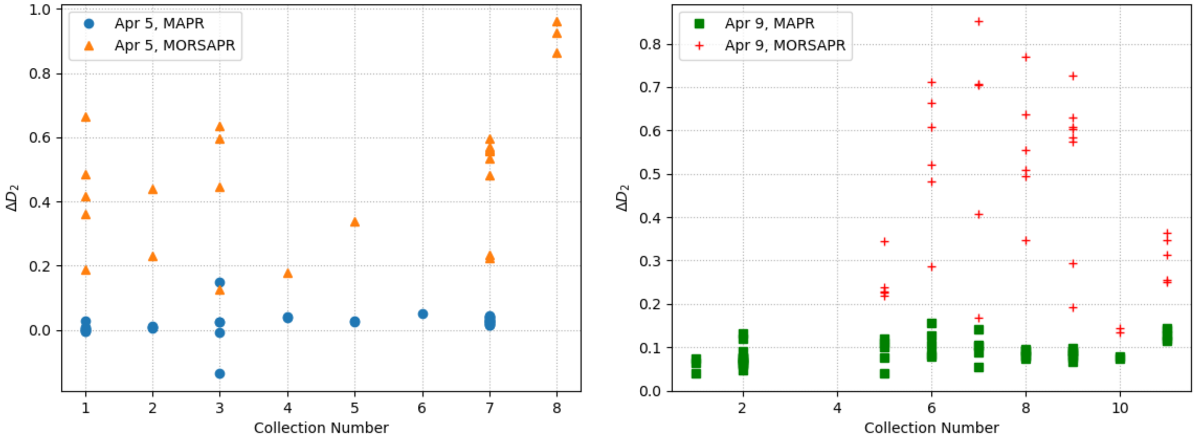

Fig. 6: Difference in measured fractal dimension by choice of threshold factor for 5 April 2019 collections (left) and 9 April 2019 collections (right) by sensor. For April 5, the mean $\Delta D_2 = 0.020 \pm 0.036$ for data collected with the MAPR sensor, and $\Delta D_2 = 0.490 \pm 0.217$ for data collected with the MORSAPR sensor. With the April 9 collections, $\Delta D_2 = 0.090 \pm 0.027$ for the MAPR data compared to $\Delta D_2 = 0.451 \pm 0.202$ for the MORSAPR data.

The Hurst exponent H is determined by fitting a power-law expression to the sequence of $(R/S)_s$ values

$$(R/S)_s = as^H \tag{7}$$

where a is a constant and s represents the size of the series [8, 9, 10, 11, 12, 13].

Figure 7 provides an example of a log-log plot of R/S vs the scale length s for data collected with the MAPR sensor in pupil mode on April 6. The total wavefront intensity summed over the entire frame was determined for each frame in the collection, and the rescaled range was then determined using the algorithm described above. A linear least-squares fit to the plotted data points provides the measured Hurst exponent $H = 0.626$.

In Figure 8, measured Hurst exponents determined in the same manner are plotted by recorded run number for selected MAPR and MORSAPR sensor data collected in pupil mode. From these cases, $H = 0.606 \pm 0.203$ for data collected on April 5 using the MAPR sensor, and $H = 0.552 \pm 0.214$ for MORSAPR data collected the same night. For the April 9 data, $H = 0.566 \pm 0.234$ from MAPR and $H = 0.606 \pm 0.226$ from MORSAPR collections.

These measurements suggest that the wavefront data collected during the ERCAOS campaign has a long range corre-

---

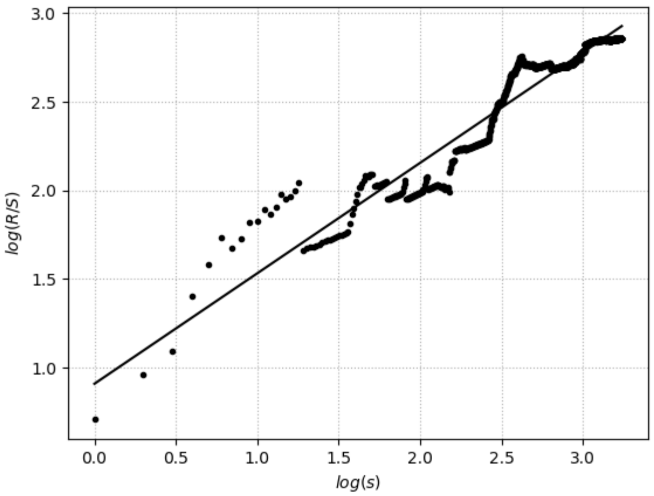

Fig. 7: Log-log plot of R/S over the scale length s. The slope of the linear least-squares fit line gives the Hurst exponent for this time series. For the time series shown, $H = 0.626$.

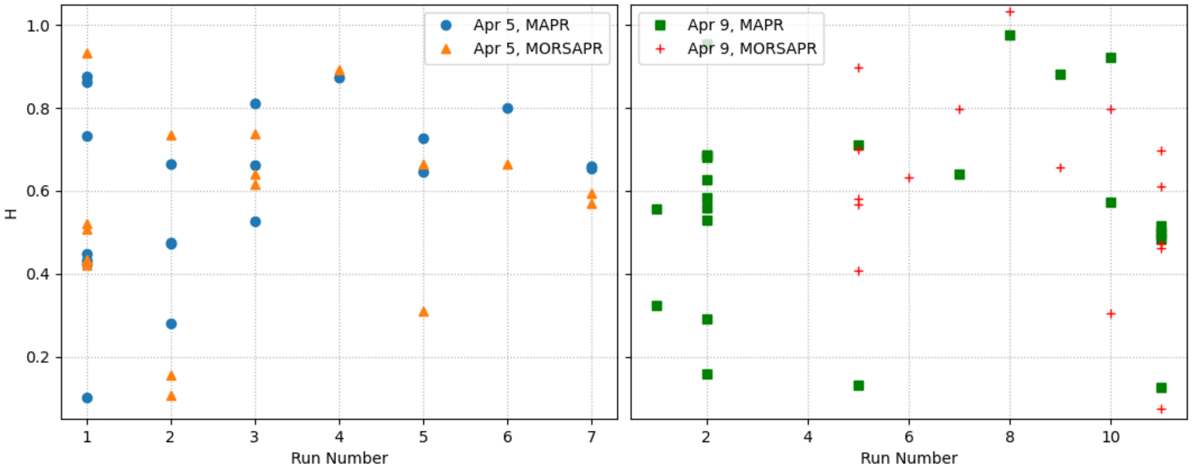

Fig. 8: Hurst exponents for selected files from April 5 (left) and April 9 (right) collections. April 5 MAPR measurements yielded a mean H of 0.606 ± 0.203 while MORSAPR measurements of $H = 0.552 \pm 0.214$. From data collected on April 9, $H = 0.566 \pm 0.234$ from MAPR measurements and $H = 0.606 \pm 0.226$ from data collected on the MORSAPR sensor.

lated structure, indicated by measurements falling within $0.5 < H < 1$. Conversely, anti-correlated structure would be signified by Hurst exponents in the range of $0 < H < 0.5$, while $H = 0.5$ indicates an uncorrelated series [7]. Long-range correlated datasets tend to cluster in a particular direction, rather than exhibiting wild randomness, with future values more likely to be influenced by earlier values.

3.3 Detrended Fluctuation Analysis

Additional fractal characterization can be achieved via detrended fractal analysis (DFA) which provides information about fractal scaling properties and long-range correlations in time-series datasets. In the simplest case, without the presence of underlying trends in the data, monofractal scaling behavior can be quantified by a single scaling exponent, the Hurst exponent. In some cases, different scaling exponents may exist over different scale regimes. And in cases where underlying trends lead to long-range correlations in a dataset, multifractal detrended fluctuation analysis (MF-

---

DFA) can be utilized to describe the scaling behavior.

As provided by Kantelhardt et al. [7], the generalized MF-DFA process for a one-dimensional time series x_k of length N is performed by first generating a series of cumulative deviations from the mean of the series

$$Y(i) \equiv \sum_{k=1}^{i} [x_k - \langle x \rangle] \tag{8}$$

for $i = 1, \ldots, N$. The profile $Y(i)$ is then divided into $2N_s$ segments; $N_s \equiv \mathrm{int}(N/s)$ non-overlapping segments of equal length s starting from $Y(1)$ and another N_s segments of length s starting from $Y(N)$ and working in the opposite direction.

A least-squares fit is used to determine the local trend for each of the $2N_s$ segments, where linear, cubic, or higher order polynomials y_ν can be considered, referred to as DFA1, DFA2, DFA3, etc. This process eliminates trends of order m-1 from the original series x_k [7].

The variance is given by

$$\sigma^2(s,\nu) \equiv \frac{1}{s} \sum_{i=1}^{s} \{Y[N - (\nu - N_s)s + i] - y_\nu(i)\}^2 \tag{9}$$

for $\nu = N_s + 1, \ldots, 2N_s$, with $y_\nu(i)$ as the fitting polynomial in segment ν. Next, the q^{th} order fluctuation function is obtained by averaging over all segments

$$F_q(s) \equiv \left\{ \frac{1}{2N_s} \sum_{\nu=1}^{2N_s} \left[F^2(s,\nu)\right]^{q/2} \right\}^{1/q} \tag{10}$$

with $q \neq 0$. Log-log plots of $F_q(s)$ versus s for various values of q can be used to illustrate the scaling behavior of the fluctuation functions. For large values of s, if x_k is long-range power-law correlated,

$$F_q(s) \sim s^{h_q} \tag{11}$$

where h_q represents the generalized Hurst exponent. For a stationary timeseries, h_2 is equivalent to the standard Hurst exponent H. A significant dependence of h_q on q indicates multifractal behavior, with small and large fluctuations scaling differently. Furthermore, one may also consider the multifractal scaling exponent τ_q which is given by

$$\tau_q = qh_q - 1. \tag{12}$$

A mono-fractal series is indicated by a linear q-dependence on τ_q while a multifractal series will exhibit a non-linear τ_q [14].

The MF-DFA method produces inaccurate results when working with a strong anti-correlated time series, where h_q approaches zero. A modified technique, which involves integrating the time series before performing the MF-DFA, can be utilized to produce reliable generalized Hurst exponents in these cases [7]. Here Equation 8 is replaced by a double summation,

$$\tilde{Y}(i) \equiv \sum_{k=1}^{i} [Y(k) - \langle Y \rangle] \tag{13}$$

and the generalized fluctuation functions $\tilde{F}_q(s)$ are related to h_q by

$$\tilde{F}_q(s) \sim s^{\tilde{h}_q} = s^{h_q+1}. \tag{14}$$

Motivated by h_q values approaching zero and a poor linear fit to $\log(F_q)$ vs $\log(s)$ data, generalized Hurst exponents were also measured from $\log(\tilde{F}_q)$ in several cases as a comparison. Figure 9 shows $\log(F_q)$ vs $\log(s)$ plotted for a range of q values with linear least-squares fits superimposed. An included plot of the fit residuals shows close agreement at longer segment lengths. The $\tilde{F}_q$ case for the same data is illustrated on the right side of the same figure. Here the fit is generally improved for small segment lengths but produces slightly larger residuals at larger values of s. The resulting generalized Hurst exponent h_q and multifractal exponents τ_q are plotted in Figure 10 for various values of q. It can

---

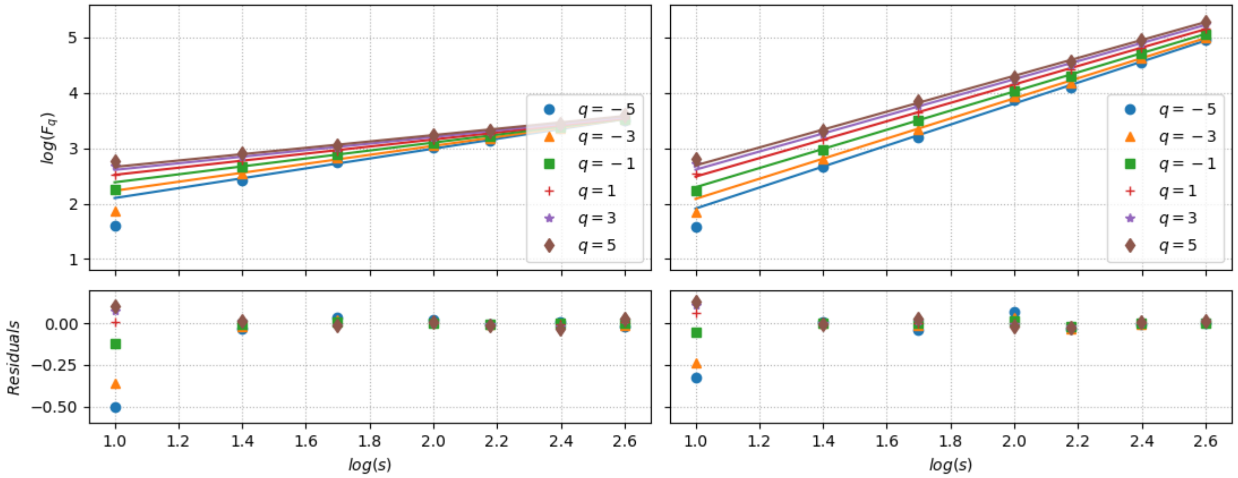

Fig. 9: Log-log plots of the MF-DFA2 fluctuation functions are shown for a range of q values as a function of s. The slopes of the linear least-squares fits shown represent the generalized Hurst exponent, with the residuals to this fit plotted beneath. The left side shows the fluctuation functions $F_q(s)$ described above, while the right side gives the modified fluctuation functions $\tilde{F}_q(s)$.

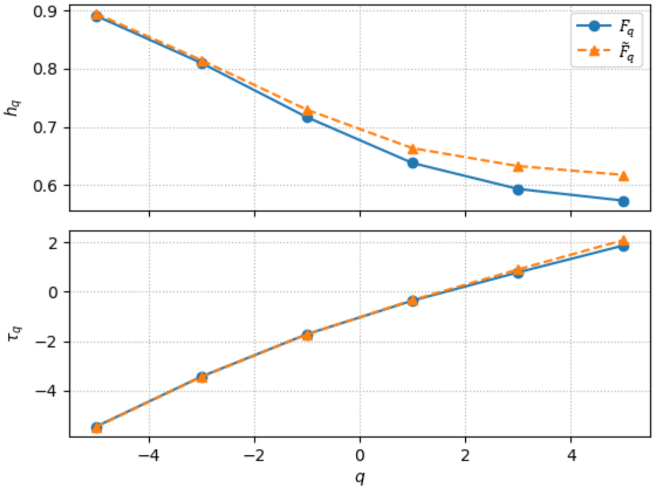

Fig. 10: Plots of the generalized Hurst exponent and multifractal scaling exponent for the fluctuation functions $F_q(s)$ and $\tilde{F}_q(s)$ shown in Figure 9. Quantities obtained via $F_q(s)$ are denoted as blue circles with a solid blue connecting line and quantities from $\tilde{F}_q(s)$ are given as orange triangles with a dashed connecting line. Both cases use MF-DFA2 segment polynomial fits y_v.

be seen that h_q and τ_q derived from either approach are in strong agreement for $q < 0$, but start to deviate for positive values of q.

When considering a range of polynomials for y_v, the trends in h_q and τ_q are very similar. Figure 11 shows DFA1, DFA2, and DFA3 trends removed for each length s segment over the same data time series. In all cases h_q is shown to vary with q; along with the non-linear profile of τ_q, this indicates a multifractal time series. Here h_2 for the DFA2 case is a very close match to $H = 0.626$ which was measured for the same example case (see Figure 8) as expected [3].

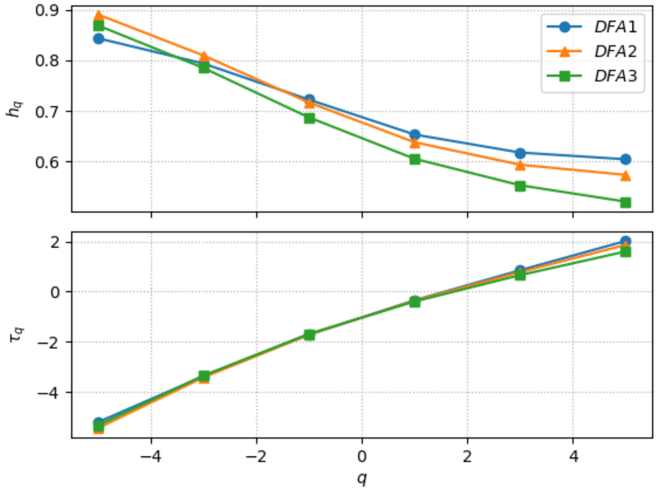

Fig. 11: The q dependence of the generalized Hurst exponent h_q (top) and corresponding multifractal scaling exponent τ_q (bottom) is shown for MF-DFA1, MF-DFA2, and MF-DFA3.

4. SUMMARY

The ERCAOS dataset contains over 400 collections of wavefront intensity measurements made during April 2019 using laser projections from the NOAA Mauna Loa observatory on Hawaii Island to receiver telescopes set up 149.2 km away at the Maui Space Surveillance Complex on Haleakalā. The two-dimensional fractal dimension D_2 has been measured using the box counting method for data collected across three different nights. Furthermore, range-scale analysis was performed on data collected over two nights. Measurements of the Hurst exponent suggest long-range correlated structure in atmospheric turbulence. This is also supported by measurements of the generalized Hurst exponent using multifractal detrended fluctuation analysis on select collections. The generalized Hurst exponent and the associated multifractal scaling exponent indicate multifractal structure in the ERCAOS turbulence profiles, which agrees with previous measurements made elsewhere.

Acknowledgement. This work has been funded by AFOSR grant #20RDCOR015.

REFERENCES

[1] P. E. Dimotakis, H. J. Catrakis, "Turbulence, fractals, and mixing," *GALCIT Report FM97-1*, (1997).

[2] H. Zhai, B. Wang, J. Zhang, A. Dang, "Fractal phase screen generation algorithm for atmospheric turbulence," *Appl. Opt.*, Vol. 54, 4023, (2015).

[3] X. Chen, X. Li, T. Luo, C. Sun, Q. Liu, W. Zhu, N. Weng, "Fractal properties of optical turbulence profiles," *Proc. SPIE 10697, Fourth Seminar on Novel Optoelectronic Detection Technology and Application, 106972O*, doi: 10.1117/12.2306138 (20 Feb 2018).

[4] M. Vorontsov, E. Polnau, T. Weyrauch, V. Kulikov, "The Extended-Range Comprehensive Atmospheric Optics Sensing (ERCAOS) Campaign: Overview," *Communications and Observations through Atmospheric Turbulence (COAT): Characterization and Mitigation*, *Internal Report*, Dec 2019. Retrieved from onera.fr/sites/default/files/actualites/agenda/2decembre2019/Day1-Talk4-Session2-VORONTSOV-ERCAOS-COAT-2019.pdf on 21 Oct 2022.

[5] M. Vorontsov, "Laser Beam & Image Propagation in Deep Turbulence Conditions: UD Effort Overview & Path Forward," *Wave Optics of Deep Atmospheric Turbulence: From Underlying Physics Towards Predictive Modeling, Mitigation, and Exploitation*, AFOSR MURI Presentation, Oct 2017. Retrieved from https://community.apan.org/cfs-file/__key/docpreview-s/00-00-02-23-40/920-Vorontsov.pdf on 21 Oct 2022.

[6] J. Li, Q. Du, C. Sun, "An improved box-counting method for image fractal dimension estimation," *Pattern Recognition*, **42 (11)**: 2460-2469 (2009).

[7] J. W. Kantelhardt, S. A. Zschiegner, E. Konscienly-Bunde, S. Havlin, A. Bunde, and H. E. Stanley, "Multifractal detrended fluctuation analysis of nonstationary time series," *Physica A* **316**, 87-114 (2002).

[8] J. Alvarez-Ramirez, J. C. Echeverria, E. Rodriguez, "Performance of a high-dimensional R/S method for Hurst exponent estimation," *Physica A* **387**:6452-6462 (2008).

[9] B. Qian, K. Rasheed, "Hurst exponent and financial market predictability," *IASTED Conference on Financial Engineering and Applications*, 203-209 (FEA 2004).

[10] J. Feder, "Fractals," *New York: Plenum Press* ISBN 978-0-306-42851-7 (1988).

[11] B. Mandelbrot, J. Wallis, "Robustness of the rescaled range R/S in the measurement of noncyclic long run statistical dependence," *Water Res.*, **5**, 967-88 (1969).

[12] H. E. Hurst, "Long-term storage capacity of reservoirs," *Amer. Soc. Civil Eng.* **116**, 770-808 (1951).

[13] C.-K. Peng, S. Buldyrev, S. Havlin, M. Simons, H. Stanley, and A. Goldberger, "Mosaic organization of dna nucleotides," *Phys. Rev. E*, **49**, 1685-89 (1994).

[14] L. and Lovallo Telesca, "Analysis of the time dynamics in wind records by means of multifractal detrended fluctuation analysis and the fishershannon information plane," *J. Stat. Mech.*, P07001 (2001).
